

Ground-state properties of the double trillium lattice antiferromagnet $\text{KBaCr}_2(\text{PO}_4)_3$

R. Kolay,¹ Qing-Ping Ding,² Y. Furukawa,² A. A. Tsirlin,³ and R. Nath^{1,*}

¹*School of Physics, Indian Institute of Science Education and Research Thiruvananthapuram-695551, India*

²*Ames National Laboratory and Department of Physics and Astronomy, Iowa State University, Ames, Iowa 50011, USA*

³*Felix Bloch Institute for Solid-State Physics, Leipzig University, 04103 Leipzig, Germany*

(Dated: July 15, 2024)

Trillium lattices formed by corner-shared triangular units are the platform for magnetic frustration in three dimensions. Herein, we report structural and magnetic properties of the Cr-based double trillium lattice material $\text{KBaCr}_2(\text{PO}_4)_3$ studied by x-ray diffraction, magnetization, heat capacity, thermal conductivity, and ^{31}P nuclear magnetic resonance (NMR) measurements complemented by density-functional band-structure calculations. Heat capacity and ^{31}P NMR measurements reveal the magnetic transition at $T_{\text{N}1} \simeq 13.5$ K in zero field followed by another transition at $T_{\text{N}2} \simeq 7$ K in weak applied fields. The NMR sublattice magnetization confirms that the transition at $T_{\text{N}1}$ is 3D in nature. The ^{31}P spin-lattice relaxation rate in the ordered state follows the T^3 behavior indicative of the two-magnon Raman process. The spin lattice of $\text{KBaCr}_2(\text{PO}_4)_3$ comprises two crystallographically nonequivalent ferromagnetic sublattices that are coupled antiferromagnetically, thus eliminating frustration in this trillium network.

I. INTRODUCTION

Frustrated magnets where configurations of localized magnetic moments do not satisfy pair-wise interactions simultaneously often have large ground-state degeneracy and realize exotic phases at low temperatures. The source of frustration could be either spin-lattice geometry with triangular loops or competing interactions between nearest neighbors (NN) and further neighbors [1]. Owing to the ground-state degeneracy, these quantum magnets evade the conventional magnetic long-range order (LRO) and serve as prime candidates to foster various nontrivial ground states such as quantum spin liquid (QSL), spin ice, and unconventional spin glass [2–4]. Over the years, significant attention has been focused in realizing frustrated magnets in two dimensions within the triangular [5] and kagome [6] geometries, whereas pyrochlore and hyperkagome lattices have been the primary frustration motifs in three dimensions (3D) [7–10].

The family of frustrated 3D magnets was recently augmented by the trillium lattice formed by corner-shared triangular motifs with six nearest neighbors. A distinctive feature of this geometry is its chiral nature that has interesting implications in itinerant systems, such as MnSi, FeGe, and MnGe with skyrmion magnetic phases [11–13] and topological Hall effect [14, 15]. $\text{Na}[\text{Mn}(\text{HCOO})_3]$, the insulating metal-organic-framework compound with the trillium geometry, exhibits a pseudo-plateau at $1/3$ of the saturation magnetization and reveals an unusual 2-k magnetic ground state [16]. A few oxide-based trillium-lattice compounds belonging to the langbeinite structure type have been investigated too. $\text{K}_2\text{Ni}_2(\text{SO}_4)_3$ with $S = 1$ moments of Ni^{2+} was shown to feature the field-induced QSL state [17] and a spinon continuum witnessed by inelastic

neutron scattering [18]. Another langbeinite-type compound $\text{KSrFe}_2(\text{PO}_4)_3$ was shown to evade long-range order already in zero field [19], whereas $\text{K}_2\text{CrTi}(\text{PO}_4)_3$ with the mixture of magnetic Cr^{3+} and nonmagnetic Ti^{4+} develops two magnetic transitions and non-trivial spin dynamics [20].

In this work, we report magnetism of the $\text{KBaCr}_2(\text{PO}_4)_3$ compound [21] that lacks the effect of magnetic dilution present in $\text{K}_2\text{CrTi}(\text{PO}_4)_3$. Interestingly, our data reveal several similarities to the diluted case, including two magnetic transitions despite the absence of frustration in this two-sublattice antiferromagnet. $\text{KBaCr}_2(\text{PO}_4)_3$ belongs to the langbeinite structure type (space group $P2_13$). Two Cr^{3+} sites form interpenetrating trillium lattices, resulting in the double-trillium-lattice structure [see Fig. 1].

II. METHODS

Polycrystalline sample of $\text{KBaCr}_2(\text{PO}_4)_3$ was prepared using the conventional solid-state method. Stoichiometric amounts of K_2CO_3 (Sigma Aldrich, 99.99%), BaCO_3 (Sigma Aldrich, 99.997%), Cr_2O_3 (Sigma Aldrich, 99.999%), and $\text{NH}_4\text{H}_2\text{PO}_4$ (Sigma Aldrich, 99.995%) were thoroughly grounded for several hours to make fine powder and pressed into pellets. These pellets were placed into a platinum crucible and preheated at 600°C for 12 hrs in air to release gases formed upon decomposition of the precursors. The obtained product was further grounded and pressed into pellets. These pellets were sealed in an evacuated quartz tube and fired at 1100°C for 24 hrs with several intermediate grindings. Phase purity of the sample was confirmed by powder x-ray diffraction (XRD) recorded using the PANalytical x-ray diffractometer ($\text{CuK}\alpha$, $\lambda_{\text{avg}} = 1.5418 \text{ \AA}$) at room temperature. Rietveld refinement for the powder XRD data (Fig. 2) was performed using the FULLPROF software package [22] with the initial structural parameters taken

* rnath@iisertvm.ac.in

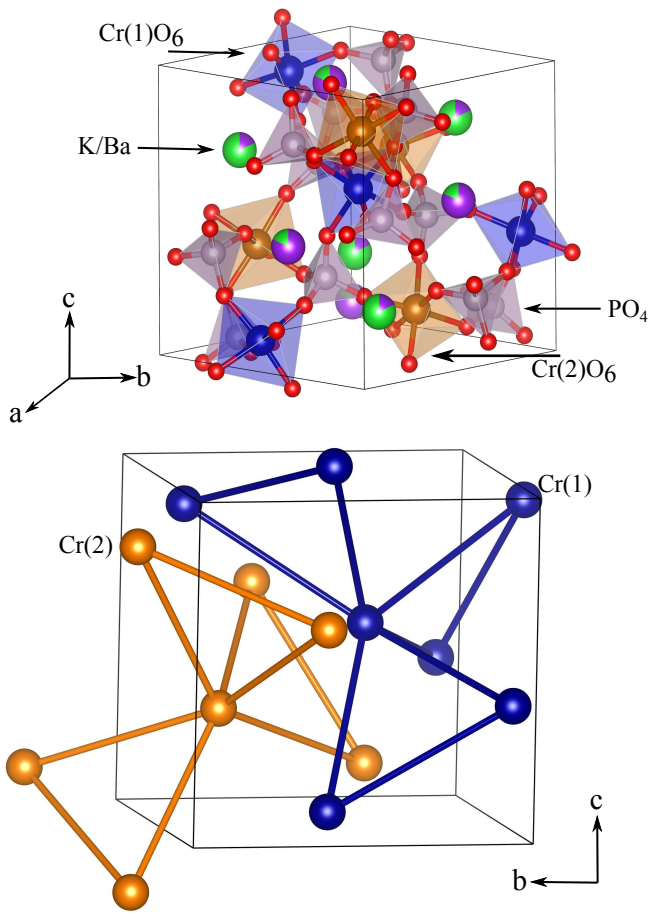


FIG. 1. (a) Crystal structure of $\text{KBaCr}_2(\text{PO}_4)_3$ featuring the $\text{Cr}(1)\text{O}_6$ and $\text{Cr}(2)\text{O}_6$ octahedra along with the PO_4 tetrahedral units. (b) Two interpenetrating trillium lattices formed by the $\text{Cr}(1)$ and $\text{Cr}(2)$ sites.

from the previous report [21]. The entire XRD pattern could be indexed using the cubic structure with the space group $P2_13$. The resulting goodness-of-fit $\chi^2 \approx 4.80$ reflects excellent sample quality. The obtained cubic lattice parameter $a \simeq 9.794 \text{ \AA}$ is in a good agreement with the literature [21].

Temperature-dependent DC magnetization (M) was measured using a vibrating sample magnetometer (VSM) attached to Physical Property Measurement System (PPMS, Quantum Design) in the temperature range 1.9 K to 380 K. AC magnetization was measured in the temperature range $2 \text{ K} \leq T \leq 15 \text{ K}$ by varying the frequency ($100 \text{ Hz} \leq \nu \leq 10 \text{ KHz}$) in an applied AC field of $H_{\text{AC}} = 5 \text{ Oe}$, using the ACMS option of PPMS. Heat capacity (C_p) as a function of temperature was measured on a small sintered pellet using the thermal relaxation technique in PPMS in different applied fields ranging from 0 to 9 T. Thermal conductivity measurement as a function of temperature was carried out on a small sintered cylindrical pellet using the two-probe method in PPMS, in the temperature range $2 \text{ K} \leq T \leq 300 \text{ K}$ and in magnetic

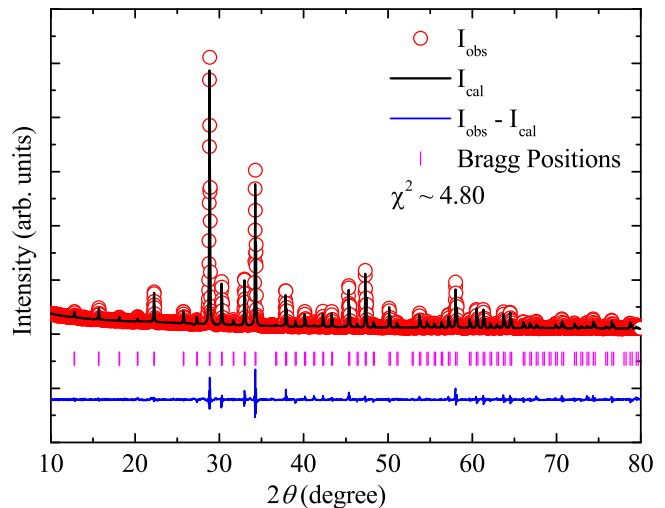


FIG. 2. Room-temperature powder XRD pattern of $\text{KBaCr}_2(\text{PO}_4)_3$. The open circles represent the experimental data and the solid red line is the Rietveld fit. Expected Bragg-peak positions are shown as pink vertical bars and the bottom line indicates the difference in intensity between the observed and experimental data.

fields up to 9 T.

Nuclear magnetic resonance (NMR) measurements were conducted using a laboratory-built phase-coherent spin-echo pulse spectrometer over the temperatures range $1.5 \text{ K} \leq T \leq 300 \text{ K}$ on the ^{31}P nucleus that has nuclear spin $I = 1/2$ and gyromagnetic ratio $\gamma_N/2\pi = 17.237 \text{ MHz/T}$. The measurements were done at four different frequencies of 8.32, 17.5, 34.1, and 127.7 MHz, which correspond to the magnetic fields of about 0.5, 1, 2, and 7 T, respectively. The NMR spectra were obtained by sweeping the magnetic field at a fixed resonance frequency. For the ^{31}P zero-shift position (H_{ref}), a non-magnetic reference sample H_3PO_4 was measured at room temperature. Then, the temperature-dependent NMR shift was calculated as $K(T) = [H_{\text{ref}} - H(T)]/H(T)$, where H is the resonance field of the sample. The nuclear spin-lattice relaxation rate ($1/T_1$) was measured at the field corresponding to the central peak position, using the standard saturation recovery technique. The nuclear spin-spin relaxation rate ($1/T_2$) was obtained by measuring the decay of the echo integral with variable spacing between the $\pi/2$ and π pulses.

Density-functional-theory (DFT) band-structure calculations were performed in the VASP [23, 24] code using the Perdew-Burke-Ernzerhof flavor of the exchange-correlation potential [25]. To account for correlation effects in the Cr $3d$ shell, the mean-field DFT+ U method was used. The value of the on-site Coulomb repulsion U_d was varied in the 2–6 eV range, whereas the Hund's coupling was fixed at $J_d = 1 \text{ eV}$, and atomic limit was used for the double-counting correction. Experimental atomic positions from Ref. [21] were utilized in all calculations.

Magnetic exchange couplings of the spin Hamiltonian

$$\mathcal{H} = \sum_{\langle ij \rangle} J_{ij} \mathbf{S}_i \cdot \mathbf{S}_j, \quad (1)$$

where $S = \frac{3}{2}$ and the summation is over atomic pairs, were evaluated by a mapping procedure [26].

Magnetic susceptibility for the resulting spin model was simulated using the quantum Monte-Carlo (QMC) loop algorithm [27] of the ALPS simulation package [28] on the finite lattice with 1728 sites and periodic boundary conditions.

III. RESULTS AND DISCUSSION

A. DC Magnetization

Temperature variation of DC magnetic susceptibility χ ($\equiv M/H$) measured in an applied field of $\mu_0 H = 0.5$ T is depicted in Fig. 3(a). As the temperature decreases, χ increases systematically and then features a broad peak at around $T_{N1} \simeq 12$ K, indicating the onset of magnetic LRO. Magnetic parameters are determined by fitting $1/\chi$ above 160 K with the Curie-Weiss (CW) law,

$$\chi(T) = \chi_0 + \frac{C}{(T - \theta_{CW})}, \quad (2)$$

where χ_0 is the T -independent susceptibility that includes core diamagnetism and Van-Vleck paramagnetism, C is the Curie constant, and θ_{CW} is the characteristic CW temperature reflecting the overall energy scale of the exchange interactions among the magnetic ions. The fit shown in the inset of Fig. 3(a) returns $\chi_0 \simeq -1.35 \times 10^{-5} \text{ cm}^3/\text{mol-Cr}^{3+}$, $C \simeq 1.63 \text{ cm}^3\text{K}/\text{mol-Cr}^{3+}$, and $\theta_{CW} \simeq -9.2$ K. From the value of C , the effective magnetic moment (μ_{eff}) was calculated using the relation $\mu_{\text{eff}} = \sqrt{3k_B C/N_A}$ to be $\sim 3.61 \mu_B$, where N_A is the Avogadro's number, k_B is the Boltzmann constant, and μ_B is Bohr magneton. For a spin-3/2 system, the spin-only effective moment is $\mu_{\text{eff}} = g\sqrt{S(S+1)} \approx 3.87 \mu_B$, assuming the Landé g -factor $g = 2$. Thus, our experimentally calculated value of μ_{eff} is indeed close to the expected value. The negative value of θ_{CW} represents dominant antiferromagnetic (AFM) interactions. The core diamagnetic susceptibility (χ_{core}) caused by the orbital motion of the core electrons is calculated to be $-2.14 \times 10^{-4} \text{ cm}^3/\text{mol}$ [29]. The Van-Vleck paramagnetic susceptibility is estimated as $\chi_{\text{VV}} \simeq 2 \times 10^{-4} \text{ cm}^3/\text{mol}$ by subtracting χ_{core} from χ_0 .

The magnetic response of $\text{KBaCr}_2(\text{PO}_4)_3$ is rather unusual, as the initial increase in the susceptibility upon approaching T_{N1} is followed by its decrease toward low temperatures. This susceptibility maximum is gradually suppressed upon increasing the field [see Fig. 3(b)], as typical for systems with a ferromagnetic ordered component. On the other hand, the magnetic isotherm (M vs

H) measured at $T = 2$ K [inset of Fig. 3(b)] is linear without any tendency toward saturation even at 9 T. It further does not show any remnant magnetization, thus identifying $\text{KBaCr}_2(\text{PO}_4)_3$ as a fully compensated antiferromagnet. The shape of χT vs T plots in Fig. 3(c) indeed imply the co-existence of FM and AFM interactions in the system [30]. Further, $\chi(T)$ measured under zero-field-cooled (ZFC) and field-cooled (FC) protocols in $\mu_0 H = 0.02$ T [inset of Fig. 3(c)] shows only a very small difference below T_N , suggesting that freezing effect play minor role in this system, in contrast to materials with structural disorder [31].

B. Heat Capacity

Figure 4(a) displays the temperature-dependent heat capacity [$C_p(T)$] measured in zero field. With lowering temperature, C_p passes through a λ -type anomaly at around $T_{N1} \simeq 12.1$ K, implying the onset of magnetic LRO. Heat capacity of an insulator contains two contributions: one is phonon/lattice contribution (C_{ph}), dominant in the high-temperature regime, while another one is magnetic contribution (C_{mag}) that dominates over C_{ph} in the low-temperature region, depending on the strength of magnetic exchange couplings. In order to separate C_{mag} from the total heat capacity C_p , we estimated C_{ph} by fitting the high-temperature data using a linear combination of one Debye and four Einstein terms as [30, 32]

$$C_{\text{ph}} = f_D C_D(\theta_D, T) + \sum_{i=1}^4 g_i C_{\text{Ei}}(\theta_{\text{Ei}}, T). \quad (3)$$

The first term in Eq. (3) is the Debye model

$$C_D(\theta_D, T) = 9nR \left(\frac{T}{\theta_D} \right)^3 \int_0^{\theta_D/T} \frac{x^4 e^x}{(e^x - 1)^2} dx, \quad (4)$$

where $x = \frac{\hbar\omega}{k_B T}$, ω is the frequency of oscillation, R denotes the universal gas constant, and θ_D is the characteristic Debye temperature. The high-energy modes of phonon vibration (optical modes) are attributed to the second term in the Eq. (3), known as the Einstein term,

$$C_{\text{E}}(\theta_{\text{E}}, T) = 3nR \left(\frac{\theta_{\text{E}}}{T} \right)^2 \frac{e^{\frac{\theta_{\text{E}}}{T}}}{(e^{\frac{\theta_{\text{E}}}{T}} - 1)^2}. \quad (5)$$

Here, θ_{E} is the characteristic Einstein temperature. The coefficients f_D , g_1 , g_2 , g_3 , and g_4 are the weight factors, which take into account the number of atoms per formula units (n). The best fit of the zero-field $C_p(T)$ data in the high-temperature region [black line in Fig. 4(a)] returns $\theta_D \simeq 80$ K, $\theta_{\text{E1}} \simeq 125$ K, $\theta_{\text{E2}} \simeq 248$ K, $\theta_{\text{E3}} \simeq 265$ K, and $\theta_{\text{E4}} \simeq 730$ K with $f_D \simeq 0.052$, $g_1 \simeq 0.050$, $g_2 \simeq 0.212$, $g_3 \simeq 0.105$, and $g_4 \simeq 0.578$. One may notice that the sum of f_D , g_1 , g_2 , g_3 , and g_4 gives a value close to one, as expected. Finally, the high-temperature fit was extrapolated down to low-temperatures and subtracted

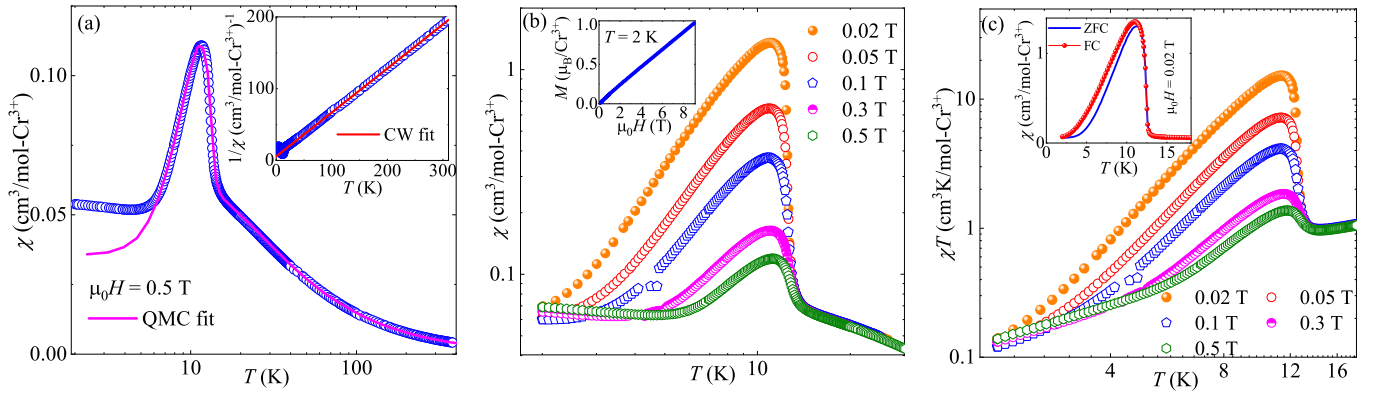


FIG. 3. (a) χ as a function of temperature measured in an applied magnetic field of $\mu_0 H = 0.5$ T. The fit represents the QMC simulation for the magnetic model with the parameters from Table I. Inset: Inverse susceptibility $1/\chi$ vs T along with the CW fit (solid line). (b) χ vs T in different magnetic fields. Inset: Magnetic isotherm (M vs H) at $T = 2$ K. (c) χT vs T in the same fields. Inset: $\chi(T)$ measured under ZFC and FC conditions in $\mu_0 H = 0.02$ T.

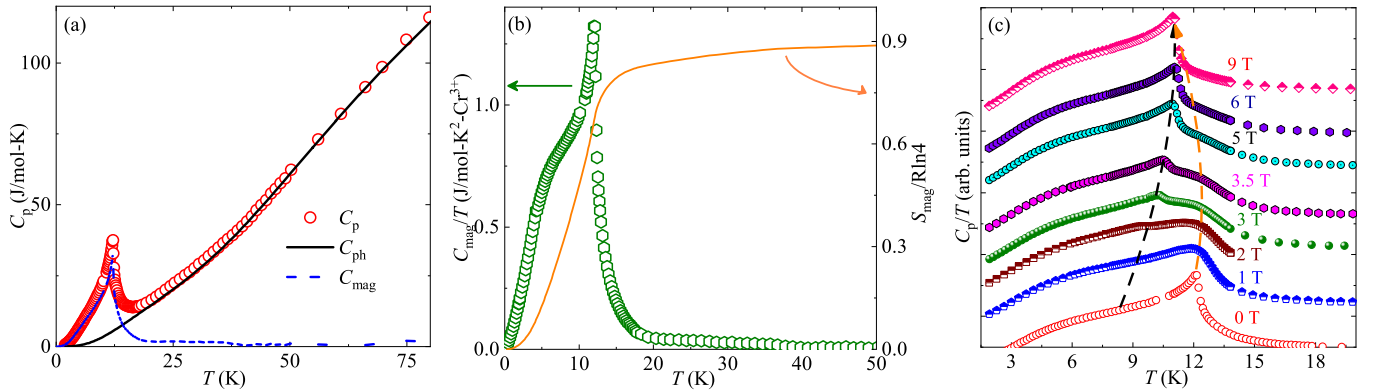


FIG. 4. (a) Zero-field heat capacity (C_p) vs T along with the Debye-Einstein fit (solid black line). The blue dotted line represents the magnetic heat capacity (C_{mag}). (b) C_{mag}/T and normalized magnetic entropy ($S_{\text{mag}}/R \ln 4$) vs T in the left and right y -axes, respectively. (c) The vertically shifted C_p/T vs T curves measured in different applied fields. The dashed lines trace the two transition points.

from the experimental $C_p(T)$ data to obtain the magnetic contribution $C_{\text{mag}}(T)$.

$C_{\text{mag}}(T)/T$ vs T is presented in the left y -axis of Fig. 4(b), which shows a sharp peak at around $T_{N1} \simeq 12.1$ K. Another broad hump is also observed below T_{N1} , which is typical for systems with higher spin [33, 34]. In order to verify the estimation of magnetic contribution, the change in magnetic entropy (ΔS_{mag}) is evaluated by integrating $C_{\text{mag}}(T)/T$ [i.e. $\Delta S_{\text{mag}} = \int_0^T \frac{C_{\text{mag}}(T')}{T'} dT'$] over the whole temperature range. As shown in the right y -axis of Fig. 4(b), the calculated value of ΔS_{mag} is ~ 10.5 J/mol-K which is close to 11.54 J/mol-K ($= R \ln 4$), expected for a spin-3/2 system.

We further measured $C_p(T)$ in different applied magnetic fields. Increasing the field shifts T_{N1} towards high temperatures, but above 2 T another peak at lower temperatures (T_{N2}) appears. Our NMR data suggest that these two features manifest two separate transitions, even though only one clear peak is seen in the heat capacity in each field. A closer inspection of the data suggests

that in fields above 2 T, the transition at T_{N1} may be manifested by a shoulder. Both transitions merge at $\mu_0 H > 6$ T. Double transitions have been reported in many frustrated magnets and can be attributed to the magnetic anisotropy [35–37].

C. AC Magnetization

To explore the possibility of the double magnetic transition in zero field, we measured magnetic susceptibility in the applied AC field of $H_{\text{ac}} = 5$ Oe at different frequencies. Figure 5(a) and (b) present the temperature variation of the real part (χ') and the imaginary part (χ''), respectively. Both χ' and χ'' show a sharp peak at $T_{N1} \simeq 12.8$ K, which is close to the anomaly observed in the zero-field $C_p(T)$ data. The peak position is independent of frequency, suggesting the absence of freezing effects. No feature associated with the second transition at T_{N2} has been observed.

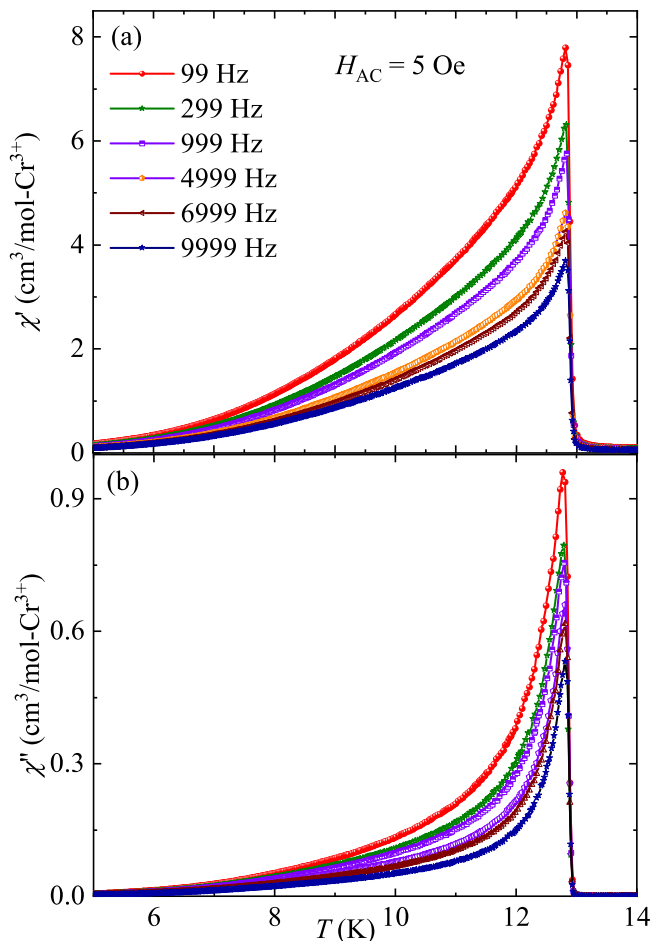


FIG. 5. (a) Real part of the AC susceptibility (χ') vs T and (b) Imaginary part of the AC susceptibility (χ'') vs T , measured at different frequencies.

D. Thermal Conductivity

In contrast to the heat-capacity data, thermal conductivity is insensitive to nuclear degrees of freedom [38] and serves as a useful probe of itinerant spin excitations at low temperatures. Figure 6 shows the temperature-dependent thermal conductivity divided by temperature (κ/T) measured in several applied fields. As temperature decreases, $\kappa(T)$ increases slowly and exhibits a step-like feature at around $T_{N1} \simeq 12.5$ K, related to the magnetic transition. No anomaly associated with the second transition at T_{N2} could be detected in zero field. As the magnetic field is applied, the step shifts with temperature [upper inset of Fig. 6], similar to that observed in the $C_p(T)$ data.

Zero-field thermal conductivity at low temperatures ($T < T_{N1}$) was fitted by $\kappa/T = a + bT^{\alpha-1}$ [38, 39]. Here, the first term represents the possible contribution of itinerant fermionic magnetic excitations, while the second term stands for conventional magnons and lattice vibrations. As shown in the lower inset of Fig. 6, the fit below

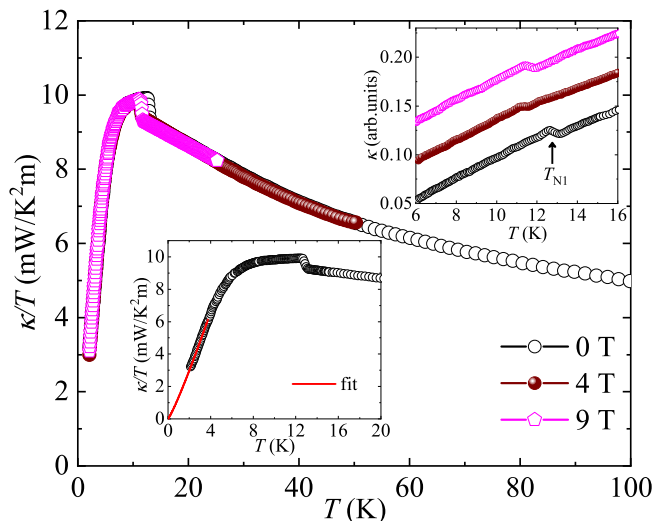


FIG. 6. κ/T vs T measured in three different applied fields. Upper inset: Vertically translated κ vs T data around T_{N1} to highlight the transition. Lower inset: Zero-field κ/T vs T in the low-temperature regime. The solid line is the fit as described in the text.

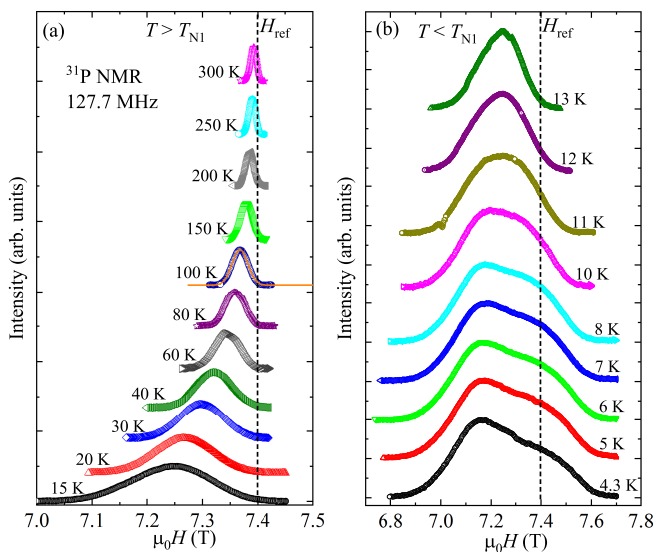


FIG. 7. Temperature-dependent ^{31}P NMR spectra, measured in an applied frequency of 127.7 MHz (a) above T_{N1} and (b) below T_{N1} . The vertical dashed line represents the nonmagnetic ^{31}P reference field.

3.5 K yields $a = 0$ with $\alpha \simeq 2.14$. One generally expects $\alpha = 3$ for both phonons and magnons in 3D. The lower value of the exponent may be due to phonon reflections at the sample surfaces or due to magnon-phonon scattering [40].

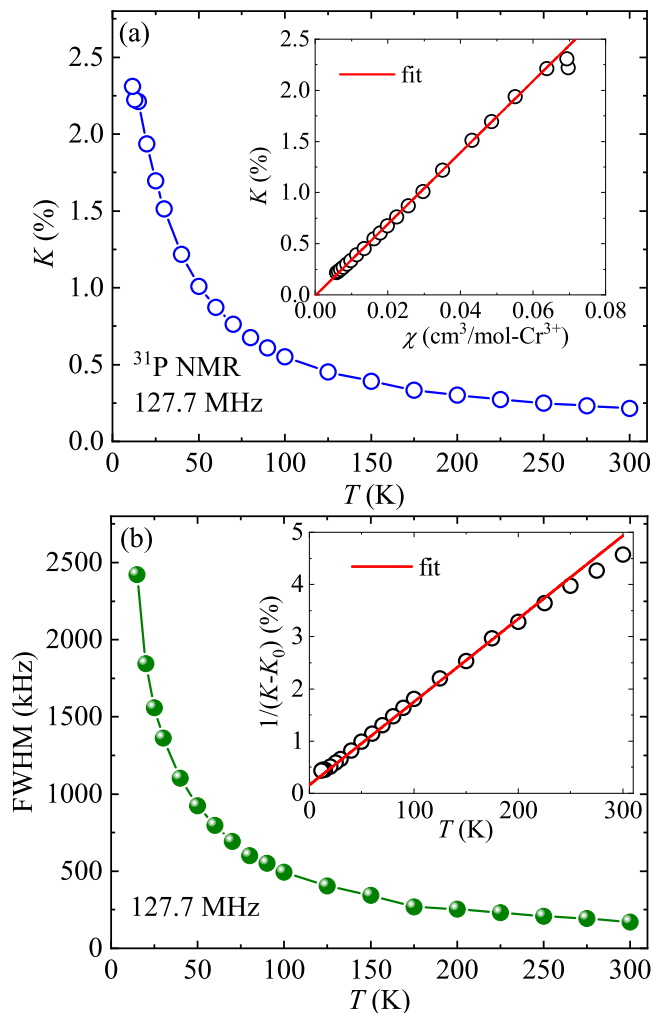


FIG. 8. (a) Temperature-dependent ^{31}P NMR shift measured at 127.7 MHz. Inset: K vs χ (measured at 2 T). The solid line is the linear fit. (b) Temperature-dependent full-width at half-maximum (FWHM). Inset: $1/(K - K_0)$ vs T and the solid line is the fit as described in the text.

E. ^{31}P NMR

We further use NMR to investigate both static and dynamic properties of the material. The $\text{KBaCr}_2(\text{PO}_4)_3$ structure features only one ^{31}P site. The $\text{Cr}(1)\text{O}_6$ and $\text{Cr}(2)\text{O}_6$ octahedra are connected via the PO_4 tetrahedra [see Fig. 1(a)]. Therefore, the ^{31}P site serves as a convenient local probe of the Cr^{3+} magnetism.

1. ^{31}P NMR Spectra

Field-sweep ^{31}P NMR spectra measured at the radio frequency of 127.7 MHz are shown in Fig. 7. The single spectral line is consistent with the unique ^{31}P site. At high temperatures, the spectrum is narrow. As the temperature decreases, the line broadens and becomes

asymmetric, as typical of polycrystalline samples due to the effects of asymmetric hyperfine coupling and/or anisotropic susceptibility [41]. The line position also shifts towards lower magnetic fields with decreasing temperature. To visualize temperature-induced changes in the line broadening and line shift, each spectrum is normalized using the peak amplitude and vertically offset in Fig. 7.

The NMR shift $K(T)$ plotted in Fig. 8(a) strongly resembles the bulk $\chi(T)$ data, thus proving the absence of any significant impurity contribution because the NMR shift probes local magnetic susceptibility (χ_{spin}). Their relation can be expressed as

$$K(T) = K_0 + \frac{A_{\text{hf}}}{N_A} \chi_{\text{spin}}(T) \quad (6)$$

where K_0 is the temperature-independent chemical shift, and A_{hf} is the hyperfine coupling constant between the ^{31}P nuclear spin and Cr^{3+} electronic spins. The linear fit of K vs χ in the inset of Fig. 8(a) returns $K_0 \simeq -0.009\%$ and $A_{\text{hf}} \simeq 1970.6 \text{ Oe}/\mu_{\text{B}}$. Temperature variation of $1/(K - K_0)$ is shown in the inset of Fig. 8(b). The data in the T -range from 50 K to 250 K are fitted using the CW law, $K = K_0 + B/(T - \theta_{\text{CW}}^K)$. The effective moment determined from the B value is $\mu_{\text{eff}}^K \simeq 3.77 \mu_{\text{B}}$ in a very good agreement with the expected value for spin-3/2 [42]. Similarly, the resulting value of $\theta_{\text{CW}}^K \simeq -10 \text{ K}$ is also in close agreement with the results of the $\chi(T)$ analysis. The full-width at half-maximum (FWHM) [Fig. 8(b)] increases slowly on cooling and diverges on approaching T_{N1} , indicating the growth of internal static fields.

2. ^{31}P spin-lattice relaxation rate $1/T_1$

The ^{31}P spin-lattice relaxation rate $1/T_1$ was measured at the field corresponding to the central peak position down to 1.5 K at four different frequencies 8.32 MHz, 17.5 MHz, 34.1 MHz, and 127.7 MHz. Typically, for an $I = 1/2$ nucleus, the recovery of the longitudinal magnetization should follow a single exponential function

$$1 - \frac{M(t)}{M(\infty)} = Ae^{-t/T_1}, \quad (7)$$

where $M(t)$ is the nuclear magnetization at a time t after the saturation pulse, and $M(\infty)$ is the equilibrium value of magnetization. The recovery curves for 127.7 MHz at four different temperatures along with the fits using the Eq. (7) are shown in Fig. 9(a).

The extracted temperature variation of $1/T_1$ is depicted in Fig. 9(b) for 8.32, 17.5, and 34.1 MHz. At high temperatures ($T \geq 20 \text{ K}$), $1/T_1$ is almost temperature-independent as the moments are fluctuating fast and randomly in the paramagnetic regime [43]. At low temperatures, two anomalies in $1/T_1(T)$ appear: a sharp kink at T_{N1} is followed by a weak anomaly T_{N2} that confirms two successive magnetic transitions in finite magnetic fields. The anomaly at $T_{\text{N1}} \simeq 13.5 \text{ K}$ remains

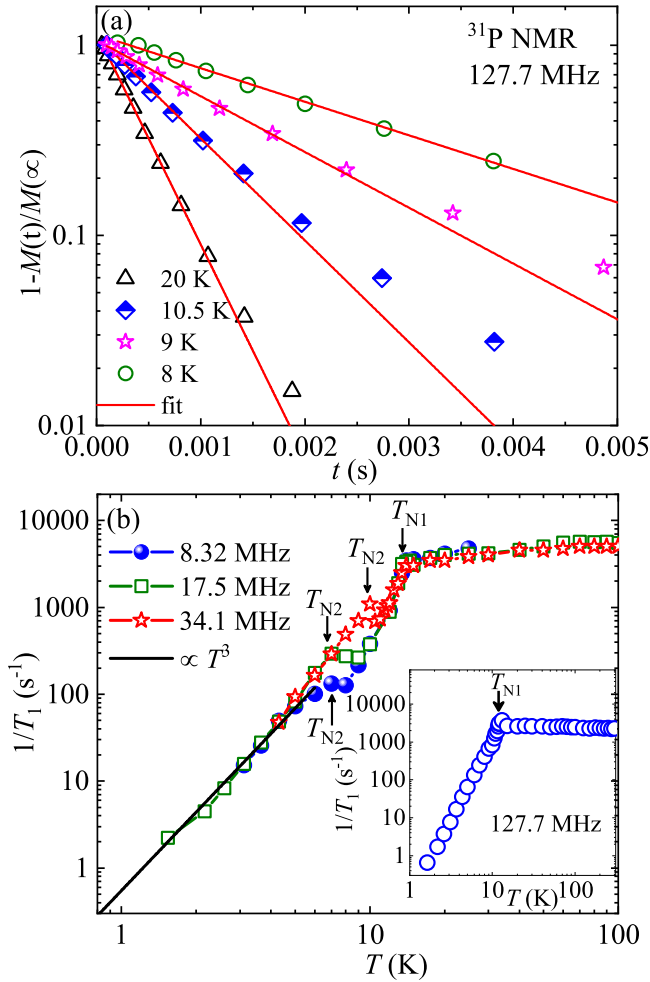


FIG. 9. (a) Longitudinal magnetization recovery curves measured at 127.7 MHz for four selected temperatures. Solid lines are the fits using Eq. (7). (b) Temperature variation of the ^{31}P spin-lattice relaxation rate, $1/T_1$, at three different frequencies, 8.32 MHz, 34.1 MHz, and 17.5 MHz. The arrows mark two successive magnetic transitions at T_{N1} and T_{N2} . The solid line represents the T^3 fit below T_{N2} . Inset: $1/T_1$ vs T at 127.7 MHz.

almost frequency-independent, whereas the one at T_{N2} moves toward higher temperatures with increasing frequency ($T_{N2} \sim 7$ K, ~ 7.5 K, and ~ 10 K for 8.32 MHz, 17.5 MHz, and 34.1 MHz, respectively). These results are consistent with those found from the heat capacity data. Below T_{N2} , $1/T_1$ decreases toward zero as a result of the melting of the critical fluctuations in the ordered state and scattering of magnons by nuclear spins [44, 45]. The $1/T_1$ vs T measured at 127.7 MHz [inset of Fig. 8(b)] exhibits only one peak at around $T_{N1} \simeq 13.5$ K suggesting that the two transitions are merged into one in higher fields.

In the ordered state ($T < T_N$) and for $T \gg \Delta/k_B$ (Δ is the energy gap in the acoustic magnon spectrum), $1/T_1$ either obeys the T^3 behavior due to a two-magnon Raman process or the T^5 behavior due to a three magnon

process [46]. Clearly, the T^3 behavior of $1/T_1$ below T_{N2} [see Fig. 9(b)] suggests that the relaxation is dominated by two-magnon processes in this compound. Similar behavior is also reported in several other low-dimensional or frustrated magnets [36, 44].

From the high-temperature part of $1/T_1$, one can estimate the effective exchange coupling between the Cr^{3+} moments as [43, 47],

$$\left(\frac{1}{T_1}\right)_{T \rightarrow \infty} = \frac{(\gamma_N g \mu_B)^2 \sqrt{2\pi} z' S(S+1)}{3\omega_{\text{ex}}} \left(\frac{A_z}{z'}\right)^2. \quad (8)$$

Here, $\omega_{\text{ex}} = (J_{\text{max}} k_B / \hbar) \sqrt{2zS(S+1)/3}$ is the Heisenberg exchange energy, $z = 6$ is the number of nearest-neighbor spins of each Cr^{3+} ion assuming the trillium-lattice geometry, and $z' = 4$ represents the number of nearest-neighbor Cr^{3+} spins for a given P site. Using the relevant parameters, $A_z \simeq 1970.6$ Oe/ μ_B , $\gamma_N = 108.28$ rad s^{-1} Oe $^{-1}$, $g = 2$, $S = 1/2$, and the high-temperature (150 K) relaxation rate of $\left(\frac{1}{T_1}\right)_{T \rightarrow \infty} \simeq 2325$ s^{-1} , the magnitude of the maximum exchange coupling constant is calculated to be $J_{\text{max}}/k_B \simeq 1.21$ K. This is consistent with the average value of the exchange couplings estimated from the band-structure calculations.

3. ^{31}P spin-spin relaxation rate $1/T_2$

The ^{31}P spin-spin relaxation rate ($1/T_2$) was recorded by monitoring the decay of the transverse magnetization (M_{xy}) after a $\pi/2 - \tau - \pi$ pulse sequence as a function of the pulse separation time τ . The M_{xy} can be fitted using the following exponential function

$$M_{xy} = M_0 e^{-2\tau/T_2}. \quad (9)$$

The recovery curves at 17.5 MHz for a few selected temperatures are presented in Fig. 10(a). The obtained $1/T_2$ from the fit using Eq. (9) as a function of temperature is shown in Fig. 10(b) for two different frequencies. At low temperatures, it exhibits two anomalies for both frequencies. The anomaly at $T_{N1} \simeq 13.5$ K remains unchanged, whereas T_{N2} shifts toward higher temperatures ($T_{N2} \simeq 7$ K and 7.5 K for 8.32 MHz and 17.5 MHz, respectively) with increasing frequency, similar to that observed in the $1/T_1$ measurements.

4. Low- T spectra

In order to understand the nature of transitions, we measured ^{31}P NMR spectra in the low-temperature regime and in a lower frequency of 34.1 MHz. Usually NMR spectrum becomes broader with increasing magnetic field in a power sample if the distribution of the hyperfine fields originating from the anisotropy in the hyperfine coupling constant and/or the magnetic susceptibility. Therefore, measurements in a lower field (and,

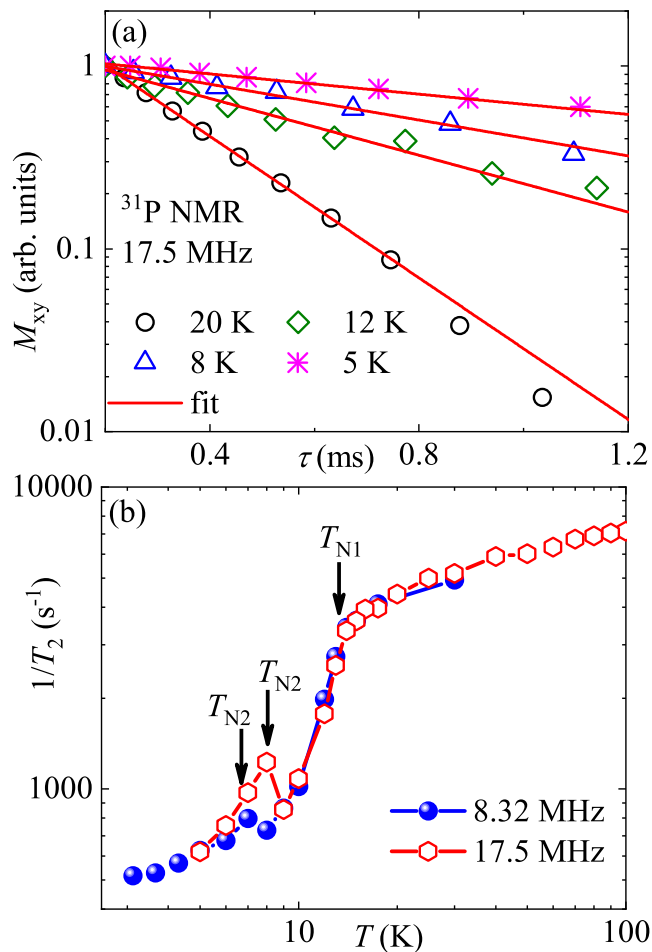


FIG. 10. (a) Transverse magnetization recovery curves as a function of τ at four different temperatures measured at 17.5 MHz. (b) $1/T_2$ vs T . The downward arrows mark two magnetic transitions.

correspondingly, at a lower frequency) may provide the intrinsic NMR line shape [48, 49]. As shown in Fig. 11, the spectral width at 34.1 MHz is reduced drastically as compared to 127.7 MHz. Further, the NMR line is found to broaden systematically with decreasing temperature. Below T_{N1} , it broadens abruptly due to the development of static internal magnetic field in the LRO state [35]. At very low temperatures, though, no significant line broadening is observed but the line width remains almost unchanged below about 10 K, which matches with the value of T_{N2} . From the shape of the powder NMR spectra, it is often possible to deduce the nature of the ordered phase. For instance, a nearly rectangular line shape is anticipated for a commensurate magnetic ordering, while an incommensurate spin-density-wave state would produce a triangular powder pattern [35, 50–52]. Interestingly, the shape of the powder pattern in Fig. 11 below T_{N1} is neither rectangular nor completely triangular in shape. By contrast, collinear LRO has been revealed by neutron diffraction in zero field [21]. One possible explanation is

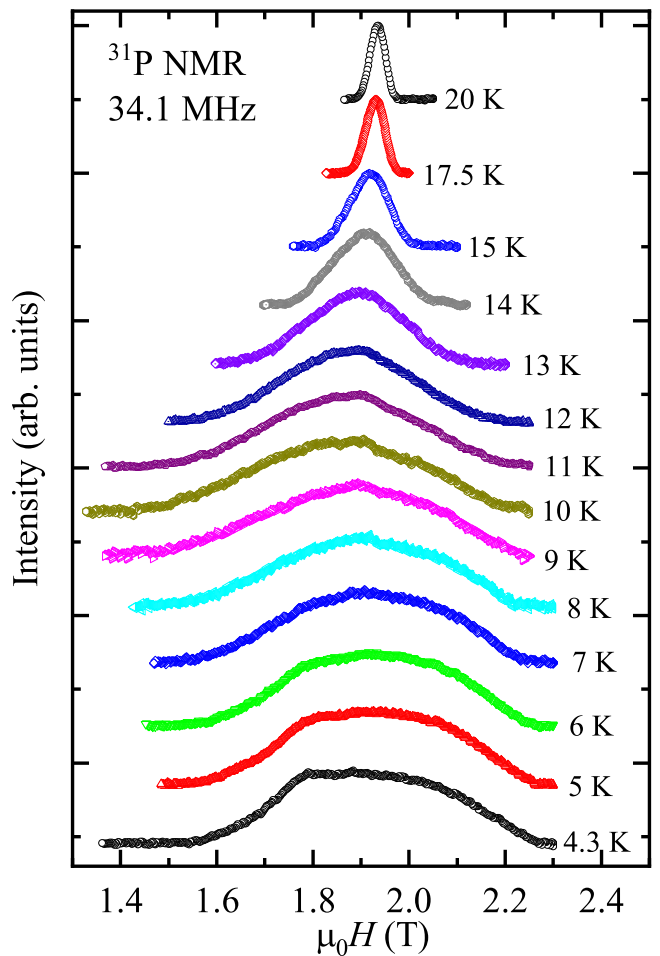


FIG. 11. ³¹P NMR spectra in the low-temperature regime measured at 34.1 MHz.

that some departure from collinearity happens below T_{N1} when magnetic field is applied.

The internal magnetic field H_{int} , which is proportional to the Cr³⁺ sublattice magnetization, was determined by taking FWHM of the spectra measured at 34.1 MHz. Below T_{N1} , this internal field increases much faster than the mean-field prediction (Fig. 12) and abruptly saturates below T_{N2} . The critical exponent of the order parameter (β) is estimated from

$$H_{\text{int}}(T) = H_0 \left(1 - \frac{T}{T_{N1}}\right)^\beta. \quad (10)$$

The fit returns $\beta \simeq 0.31$, $\mu_0 H_0 \simeq 0.59$ T, and $T_{N1} \simeq 13.9$ K. The β value is consistent with any of the 3D universality classes (Heisenberg, Ising, or XY) and reflects 3D nature of the ordering at T_{N1} [44].

F. Microscopic magnetic model

The calculated exchange couplings for $\text{KBaCr}_2(\text{PO}_4)_3$ are listed in Table I. To simplify the comparison to other

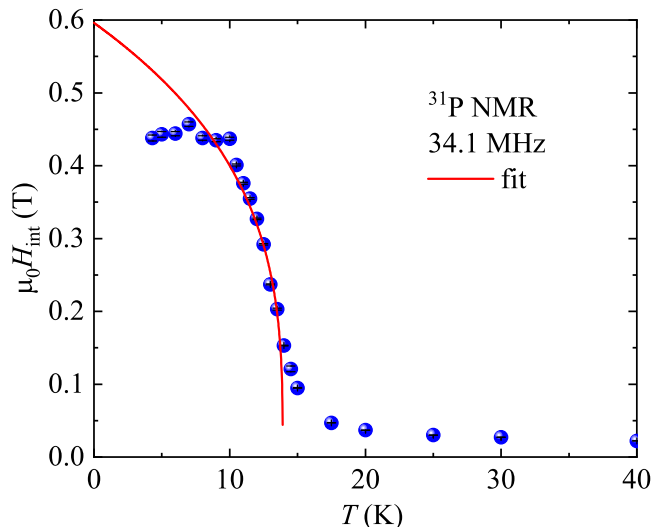


FIG. 12. Temperature-dependent internal magnetic field H_{int} obtained from the ^{31}P NMR spectra measured at 34.1 MHz in the ordered state. The solid line is the fit using Eq. (10).

langbeinite compounds, we use the same notation of $J_1 - J_5$ as in the case $\text{K}_2\text{Ni}_2(\text{SO}_4)_3$ [17] and, therefore, do not follow the hierarchy of the Cr–Cr distances in $\text{KBaCr}_2(\text{PO}_4)_3$. Interestingly, the coupling regimes of the Ni and Cr compounds are entirely different from each other. $\text{K}_2\text{Ni}_2(\text{SO}_4)_3$ features large AFM J_4 and J_5 . By contrast, the dominant terms in $\text{KBaCr}_2(\text{PO}_4)_3$ are J_1 and J_2 , both AFM. On the other hand, J_4 is negligible, whereas J_3 and J_5 are weakly FM. This coupling regime eliminates the frustration of the double-trillium spin lattice. A simple two-sublattice $\mathbf{k} = 0$ order with opposite spin directions on Cr1 and Cr2 satisfies all exchange couplings in this material [Fig. 12(a,b)]. Such a ground state has been indeed observed experimentally by neutron diffraction [21]. We further checked the dependence of magnetic couplings on the U_d parameter of DFT+ U and found that this non-frustrated coupling regime persists within the realistic windows of the U_d values [Fig. 12(c)].

The best agreement with the experimental Curie-Weiss temperature is found at $U_d = 5$ eV ($\theta_{\text{CW}} = -9.2$ K averaged over the two Cr sites), which is slightly above the typical U_d values of 3 – 4 eV employed in the previous studies of Cr^{3+} magnets [53, 54]. We further simulated magnetic susceptibility for the spin lattice with the exchange couplings $J_1 - J_5$ using QMC. The values listed in Table I allow a very accurate description of the experimental susceptibility data and show a good match with the DFT results.

Exchange fields on the Cr1 and Cr2 sites are different by virtue of the difference between J_3 and J_5 : compare $H_1 \sim J_1 + 3J_2 + 3J_4 + 6J_5 = 10.9$ K and $H_2 \sim J_1 + 3J_2 + 3J_4 + 6J_3 = 5.5$ K (at $U_d = 5$ eV). The two sublattices will thus show different temperature dependence of the magnetization, resulting in an incom-

TABLE I. The Cr–Cr distances d_i (in Å) and exchange couplings J_i (in K) for $\text{KBaCr}_2(\text{PO}_4)_3$. The J_i^{DFT} values are obtained from the DFT+ U calculations with $U_d = 5$ eV and $J_d = 1$ eV, whereas the J_i^{QMC} values are the best fit to the experimental magnetic susceptibility. The notation of Cr1 and Cr2 follows Ref. [21].

		d_i	J_i^{DFT}	J_i^{QMC}
J_1	Cr1–Cr2	4.496	4.0	3.4
J_2	Cr1–Cr2	4.919	2.9	2.5
J_3	Cr2–Cr2	6.026	−1.2	−0.9
J_4	Cr1–Cr2	5.971	0.0	0.0
J_5	Cr1–Cr1	6.084	−0.6	−0.4

plete compensation in the vicinity of T_N . This explains the abrupt increase in the magnetic susceptibility right below T_N with the eventual formation of the fully compensated state at $T \ll T_N$, where both sublattices develop equal magnetizations. Such a behavior is well reproduced by our QMC simulations [Fig. 3(a)]. Similar physics has been reported, for example, in $\text{Mn}_2\text{Mo}_3\text{O}_8$ where two magnetic sublattices are also formed by two distinct structural sublattices of the material [55, 56].

A closer inspection of the crystal structure reveals that the main exchange pathways in $\text{KBaCr}_2(\text{PO}_4)_3$, J_1 and J_2 , are those mediated by double bridges of the PO_4 tetrahedra. This coupling regime is typical for V^{4+} phosphates where double-tetrahedral bridges result in stronger superexchange couplings compared to the single-tetrahedron bridges [57]. A similar coupling regime is indeed expected in Cr^{3+} phosphates because magnetic orbitals are also t_{2g} in nature. By contrast, $\text{K}_2\text{Ni}_2(\text{SO}_4)_3$ exhibits a very different microscopic scenario because its magnetic orbitals belong to the e_g manifold. These orbitals feature a σ -overlap with oxygen p -orbitals and boost the couplings J_4 and J_5 that run via the single PO_4 tetrahedron each. We also note that only J_1 and J_2 show the typical $1/U_d$ dependence [Fig. 12(c)] expected for magnetic interactions dominated by superexchange. On the other hand, J_3 and J_5 remain almost unchanged when U_d is increased, so their ferromagnetic nature is due to the weak potential exchange in the absence of any significant contribution from superexchange.

IV. SUMMARY

In summary, we have shown that $\text{KBaCr}_2(\text{PO}_4)_3$ manifests the nonfrustrated coupling regime caused by the interplay of ferromagnetic interactions within each Cr sublattice and antiferromagnetic interactions between these sublattices. Different exchange fields on the two sublattices give rise to an incomplete compensation and the prominent susceptibility maximum right below T_{N1} , whereas at $T \ll T_{N1}$ the system tends toward a fully compensated antiferromagnet. Despite the absence of frus-

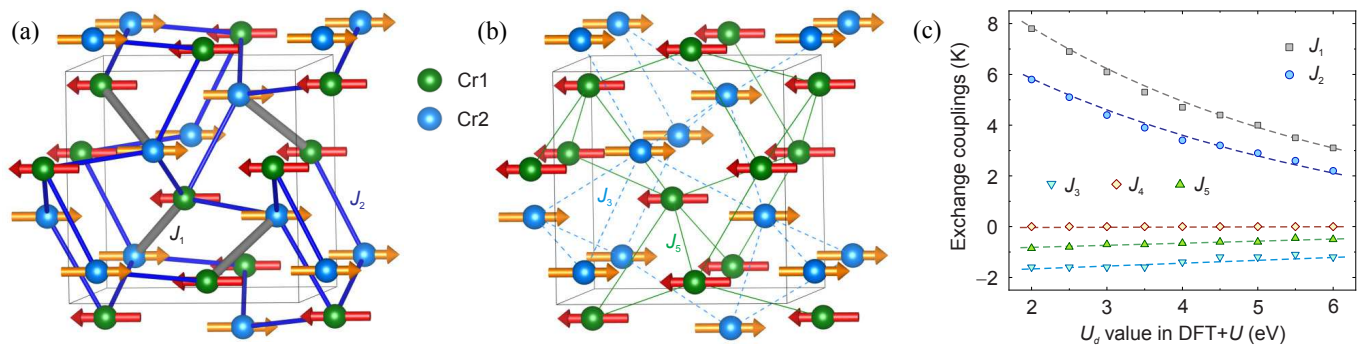


FIG. 13. (a,b) Spin lattice of $\text{KBaCr}_2(\text{PO}_4)_3$ and the $\mathbf{k} = 0$ magnetic order [21] that satisfies both AFM couplings J_1 , J_2 as well as FM coupling J_3 , J_5 . The spin direction [100] is chosen arbitrarily. (c) Exchange couplings calculated for different U_d values in DFT+ U .

tration, $\text{KBaCr}_2(\text{PO}_4)_3$ reveals further interesting features, most notably, the second magnetic transition at T_{N2} manifested by a peak in the ^{31}P spin-lattice relaxation and spin-spin relaxation rates. This second transition is clearly observed in applied fields only and may correspond to a small deviation of the magnetic order from the collinear order observed in zero field.

In the broader context of langbeinite-type compounds, $\text{KBaCr}_2(\text{PO}_4)_3$ gives an instructive example of the frustration release on the trillium lattice. All of the magnetic couplings in the langbeinite structure are long-range in nature, but they are not necessarily antiferromagnetic and, therefore, not all members of this structural family are magnetically frustrated. We also showed that the nature of the $3d$ ion determines leading magnetic interactions in the langbeinite structure.

ACKNOWLEDGMENTS

RK and RN would like to acknowledge SERB, India, for financial support bearing sanction Grant

No. CRG/2019/000960. Work at the Ames National Laboratory was supported by the U.S. Department of Energy, Office of Science, Basic Energy Sciences, Materials Sciences and Engineering Division. The Ames National Laboratory is operated for the U.S. Department of Energy by Iowa State University under Contract No. DEAC02-07CH11358. The authors gratefully acknowledge the computing time made available to them on the high-performance computer at the NHR Center of TU Dresden. This center is jointly supported by the Federal Ministry of Education and Research and the state governments participating in the NHR (www.nhrverein.de/unsere-partner).

-
- [1] A. Ramirez, Strongly geometrically frustrated magnets, *Annu. Rev. of Mater. Sci.* **24**, 453 (1994).
 [2] Y. Zhou, K. Kanoda, and T.-K. Ng, Quantum spin liquid states, *Rev. Mod. Phys.* **89**, 025003 (2017).
 [3] K. Binder and A. P. Young, Spin glasses: Experimental facts, theoretical concepts, and open questions, *Rev. Mod. Phys.* **58**, 801 (1986).
 [4] S. T. Bramwell and M. J. Gingras, Spin ice state in frustrated magnetic pyrochlore materials, *Science* **294**, 1495 (2001).
 [5] Y. Li, P. Gegenwart, and A. A. Tsirlin, Spin liquids in geometrically perfect triangular antiferromagnets, *J. Phys.: Condens. Matter* **32**, 224004 (2020).
 [6] J. S. Helton, K. Matan, M. P. Shores, E. A. Nytko, B. M. Bartlett, Y. Yoshida, Y. Takano, A. Suslov, Y. Qiu, J.-H. Chung, D. G. Nocera, and Y. S. Lee, Spin Dynamics of the Spin-1/2 Kagome Lattice Antiferromagnet $\text{ZnCu}_3(\text{OH})_6\text{Cl}_2$, *Phys. Rev. Lett.* **98**, 107204 (2007).
 [7] B. Gao, T. Chen, D. W. Tam, C.-L. Huang, K. Sasmal, D. T. Adroja, F. Ye, H. Cao, G. Sala, M. B. Stone, C. Baines, J. A. T. Verezhak, H. Hu, J.-H. Chung, X. Xu, S.-W. Cheong, M. Nallaiyan, S. Spagna, M. B. Maple, A. H. Nevidomskyy, E. Morosan, G. Chen, and P. Dai, Experimental signatures of a three-dimensional quantum spin liquid in effective spin-1/2 $\text{Ce}_2\text{Zr}_2\text{O}_7$ pyrochlore, *Nat. Phys.* **15**, 1052 (2019).
 [8] K. W. Plumb, H. J. Changlani, A. Scheie, S. Zhang, J. W. Krizan, J. A. Rodriguez-Rivera, Y. Qiu, B. Winn, R. J. Cava, and C. L. Broholm, Continuum of quantum fluctuations in a three-dimensional $S = 1$ Heisenberg magnet, *Nat. Phys.* **15**, 54 (2019).
 [9] S. Chillal, Y. Iqbal, H. O. Jeschke, J. A. Rodriguez-Rivera, R. Bewley, P. Manuel, D. Khalyavin, P. Steffens, R. Thomale, A. T. M. N. Islam, J. Reuther, and B. Lake,

- Evidence for a three-dimensional quantum spin liquid in $\text{PbCuTe}_2\text{O}_6$, *Nat. Commun.* **11**, 2348 (2020).
- [10] A. C. Shockley, F. Bert, J.-C. Orain, Y. Okamoto, and P. Mendels, Frozen State and Spin Liquid Physics in $\text{Na}_4\text{Ir}_3\text{O}_8$: An NMR Study, *Phys. Rev. Lett.* **115**, 047201 (2015).
- [11] S. Mühlbauer, B. Binz, F. Jonietz, C. Pfleiderer, A. Rosch, A. Neubauer, R. Georgii, and P. Böni, Skyrmion lattice in a chiral magnet, *Science* **323**, 915 (2009).
- [12] T. Nakajima, H. Oike, A. Kikkawa, E. P. Gilbert, N. Booth, K. Kakurai, Y. Taguchi, Y. Tokura, F. Kagawa, and T. Hisa Arima, Skyrmion lattice structural transition in MnSi , *Sci. Adv.* **3**, e1602562 (2017).
- [13] X. Z. Yu, N. Kanazawa, Y. Onose, K. Kimoto, W. Z. Zhang, Y. Ishiwata, S. Matsui, and Y. Tokura, Near room-temperature formation of a skyrmion crystal in thin-films of the helimagnet FeGe , *Nature Mater.* **10**, 106 (2011).
- [14] A. Neubauer, C. Pfleiderer, B. Binz, A. Rosch, R. Ritz, P. G. Niklowitz, and P. Böni, Topological hall effect in the A phase of MnSi , *Phys. Rev. Lett.* **102**, 186602 (2009).
- [15] N. Kanazawa, Y. Onose, T. Arima, D. Okuyama, K. Ohoyama, S. Wakimoto, K. Kakurai, S. Ishiwata, and Y. Tokura, Large Topological Hall Effect in a Short-Period Helimagnet MnGe , *Phys. Rev. Lett.* **106**, 156603 (2011).
- [16] J. M. Bulléd, J. A. M. Paddison, A. Wildes, E. Lhotel, S. J. Cassidy, B. Pato-Doldán, L. C. Gómez-Aguirre, P. J. Saines, and A. L. Goodwin, Geometric Frustration on the Trillium Lattice in a Magnetic Metal-Organic Framework, *Phys. Rev. Lett.* **128**, 177201 (2022).
- [17] I. Živković, V. Favre, C. Salazar Mejia, H. O. Jeschke, A. Magrez, B. Dabholkar, V. Nocolak, R. S. Freitas, M. Jeong, N. G. Hegde, L. Testa, P. Babkevich, Y. Su, P. Manuel, H. Luetkens, C. Baines, P. J. Baker, J. Wosnitza, O. Zaharko, Y. Iqbal, J. Reuther, and H. M. Rønnow, Magnetic Field Induced Quantum Spin Liquid in the Two Coupled Trillium Lattices of $\text{K}_2\text{Ni}_2(\text{SO}_4)_3$, *Phys. Rev. Lett.* **127**, 157204 (2021).
- [18] W. Yao, Q. Huang, T. Xie, A. Podlesnyak, A. Brassington, C. Xing, R. S. D. Mudiyansele, H. Wang, W. Xie, S. Zhang, M. Lee, V. S. Zapf, X. Bai, D. A. Tennant, J. Liu, and H. Zhou, Continuous Spin Excitations in the Three-Dimensional Frustrated Magnet $\text{K}_2\text{Ni}_2(\text{SO}_4)_3$, *Phys. Rev. Lett.* **131**, 146701 (2023).
- [19] K. Boya, K. Nam, K. Kargeti, A. Jain, R. Kumar, S. K. Panda, S. M. Yusuf, P. L. Paulose, U. K. Voma, E. Kermarrec, K. H. Kim, and B. Koteswararao, Signatures of spin-liquid state in a 3D frustrated lattice compound $\text{KSrFe}_2(\text{PO}_4)_3$ with $S = 5/2$, *APL Materials* **10**, 101103 (2022).
- [20] J. Khatua, S. Lee, G. Ban, M. Uhlarz, G. S. Murugan, R. Sankar, K.-Y. Choi, and P. Khuntia, Magnetism and spin dynamics of the $S = \frac{3}{2}$ frustrated trillium lattice compound $\text{K}_2\text{CrTi}(\text{PO}_4)_3$, *Phys. Rev. B* **109**, 184432 (2024).
- [21] P. Battle, T. Gibb, S. Nixon, and W. Harrison, The magnetic properties of the synthetic langbeinite $\text{KBaCr}_2(\text{PO}_4)_3$, *J. Solid State Chem.* **75**, 21 (1988).
- [22] J. R. Carvajal, Recent advances in magnetic structure determination by neutron powder diffraction, *Physica B: Condens. Matter* **192**, 55 (1993).
- [23] G. Kresse and J. Furthmüller, Efficiency of *ab-initio* total energy calculations for metals and semiconductors using a plane-wave basis set, *Computational Materials Science* **6**, 15 (1996).
- [24] G. Kresse and J. Furthmüller, Efficient iterative schemes for *ab initio* total-energy calculations using a plane-wave basis set, *Phys. Rev. B* **54**, 11169 (1996).
- [25] J. P. Perdew, K. Burke, and M. Ernzerhof, Generalized gradient approximation made simple, *Phys. Rev. Lett.* **77**, 3865 (1996).
- [26] H. J. Xiang, E. J. Kan, S.-H. Wei, M.-H. Whangbo, and X. G. Gong, Predicting the spin-lattice order of frustrated systems from first principles, *Phys. Rev. B* **84**, 224429 (2011).
- [27] S. Todo and K. Kato, Cluster algorithms for general- S quantum spin systems, *Phys. Rev. Lett.* **87**, 047203 (2001).
- [28] A. F. Albuquerque, F. Alet, P. Corboz, P. Dayal, A. Feiguin, S. Fuchs, L. Gamper, E. Gull, S. Gürtler, A. Honecker, R. Igarashi, M. Körner, A. Kozhevnikov, A. Läuchli, S. R. Manmana, M. Matsumoto, I. P. McCulloch, F. Michel, R. M. Noack, G. Pawłowski, L. Pollet, T. Pruschke, U. Schollwöck, S. Todo, S. Trebst, M. Troyer, P. Werner, and S. Wessel, The ALPS project release 1.3: Open-source software for strongly correlated systems, *J. Magn. Magn. Mater.* **310**, 1187 (2007).
- [29] G. A. Bain and J. F. Berry, Diamagnetic Corrections and Pascal's Constants, *J. Chem. Educ.* **85**, 532 (2008).
- [30] S. Mohanty, A. Magar, V. Singh, S. S. Islam, S. Guchhait, A. Jain, S. M. Yusuf, A. A. Tsirlin, and R. Nath, Double magnetic transitions, complex field-induced phases, and large magnetocaloric effect in the frustrated garnet compound $\text{Mn}_3\text{Cr}_2\text{Ge}_3\text{O}_{12}$, *Phys. Rev. B* **109**, 134401 (2024).
- [31] P. Bag, P. R. Baral, and R. Nath, Cluster spin-glass behavior and memory effect in $\text{Cr}_{0.5}\text{Fe}_{0.5}\text{Ga}$, *Phys. Rev. B* **98**, 144436 (2018).
- [32] E. Gopal, *Specific heats at low temperatures* (Springer Science & Business Media, 2012).
- [33] D. C. Johnston, R. J. McQueeney, B. Lake, A. Honecker, M. E. Zhitomirsky, R. Nath, Y. Furukawa, V. P. Antropov, and Y. Singh, Magnetic exchange interactions in BaMn_2As_2 : A case study of the J_1 - J_2 - J_c Heisenberg model, *Phys. Rev. B* **84**, 094445 (2011).
- [34] R. Nath, K. M. Ranjith, B. Roy, D. C. Johnston, Y. Furukawa, and A. A. Tsirlin, Magnetic transitions in the spin- $\frac{5}{2}$ frustrated magnet BiMn_2PO_6 and strong lattice softening in BiMn_2PO_6 and BiZn_2PO_6 below 200 K, *Phys. Rev. B* **90**, 024431 (2014).
- [35] K. M. Ranjith, R. Nath, M. Majumder, D. Kasinathan, M. Skoulatos, L. Keller, Y. Skourski, M. Baenitz, and A. A. Tsirlin, Commensurate and incommensurate magnetic order in spin-1 chains stacked on the triangular lattice in $\text{Li}_2\text{NiW}_2\text{O}_8$, *Phys. Rev. B* **94**, 014415 (2016).
- [36] S. Mohanty, J. Babu, Y. Furukawa, and R. Nath, Structural and double magnetic transitions in the frustrated spin- $\frac{1}{2}$ capped-kagome antiferromagnet $(\text{RbCl})\text{Cu}_5\text{P}_2\text{O}_{10}$, *Phys. Rev. B* **108**, 104424 (2023).
- [37] S. Lal, S. J. Sebastian, S. S. Islam, M. P. Saravanan, M. Uhlarz, Y. Skourski, and R. Nath, Double magnetic transitions and exotic field-induced phase in the triangular lattice antiferromagnets $\text{Sr}_3\text{Co}(\text{Nb}, \text{Ta})_2\text{O}_9$, *Phys. Rev. B* **108**, 014429 (2023).

- [38] M. Yamashita, N. Nakata, Y. Senshu, M. Nagata, H. M. Yamamoto, R. Kato, T. Shibauchi, and Y. Matsuda, Highly mobile gapless excitations in a two-dimensional candidate quantum spin liquid, *Science* **328**, 1246 (2010).
- [39] Y. Huang, D. Dai, C. Zhao, J. Ni, L. Wang, B. Pan, B. Gao, P. Dai, and S. Li, Thermal conductivity of triangular-lattice antiferromagnet $\text{Na}_2\text{BaCo}(\text{PO}_4)_2$: Absence of itinerant fermionic excitations, arXiv preprint arXiv:2206.08866 [10.48550/arXiv.2206.08866](https://arxiv.org/abs/10.48550/arXiv.2206.08866) (2022).
- [40] S. Guang, N. Li, R. L. Luo, Q. Huang, Y. Wang, X. Yue, K. Xia, Q. Li, X. Zhao, G. Chen, H. Zhou, and X. Sun, Thermal transport of fractionalized antiferromagnetic and field-induced states in the Kitaev material $\text{Na}_2\text{Co}_2\text{TeO}_6$, *Phys. Rev. B* **107**, 184423 (2023).
- [41] A. Yogi, N. Ahmed, R. Nath, A. A. Tsirlin, S. Kundu, A. V. Mahajan, J. Sichelschmidt, B. Roy, and Y. Furukawa, Antiferromagnetism of $\text{Zn}_2\text{VO}(\text{PO}_4)_2$ and the dilution with Ti^{4+} , *Phys. Rev. B* **91**, 024413 (2015).
- [42] R. Nath, A. A. Tsirlin, E. E. Kaul, M. Baenitz, N. Büttgen, C. Geibel, and H. Rosner, Strong frustration due to competing ferromagnetic and antiferromagnetic interactions: Magnetic properties of $\text{M}(\text{VO})_2(\text{PO}_4)_2$ ($M = \text{Ca}$ and Sr), *Phys. Rev. B* **78**, 024418 (2008).
- [43] T. Moriya, Nuclear Magnetic Relaxation in Antiferromagnetics, *Prog. Theor. Phys.* **16**, 23 (1956).
- [44] R. Nath, Y. Furukawa, F. Borsa, E. E. Kaul, M. Baenitz, C. Geibel, and D. C. Johnston, Single-crystal ^{31}P NMR studies of the frustrated square-lattice compound $\text{Pb}_2\text{VO}(\text{PO}_4)_2$, *Phys. Rev. B* **80**, 214430 (2009).
- [45] M. Belesi, F. Borsa, and A. K. Powell, Evidence for spin-wave excitations in the long-range magnetically ordered state of a Fe_{19} molecular crystal from proton NMR, *Phys. Rev. B* **74**, 184408 (2006).
- [46] D. Beeman and P. Pincus, Nuclear spin-lattice relaxation in magnetic insulators, *Phys. Rev.* **166**, 359 (1968).
- [47] S. Guchhait, D. V. Ambika, Q.-P. Ding, M. Uhlarz, Y. Furukawa, A. A. Tsirlin, and R. Nath, Deformed spin- $\frac{1}{2}$ square lattice in antiferromagnetic $\text{NaZnVOPO}_4(\text{HPO}_4)$, *Phys. Rev. B* **106**, 024426 (2022).
- [48] L. E. Drain, The Broadening of Magnetic Resonance Lines due to Field Inhomogeneities in Powdered Samples, *Proc. Phys. Soc.* **80**, 1380 (1962).
- [49] R. Nath, A. V. Mahajan, N. Büttgen, C. Kegler, A. Loidl, and J. Bobroff, Study of one-dimensional nature of $S = 1/2$ $(\text{Sr}, \text{Ba})_2\text{Cu}(\text{PO}_4)_2$ and BaCuP_2O_7 via ^{31}P NMR, *Phys. Rev. B* **71**, 174436 (2005).
- [50] J. Kikuchi, K. Ishiguchi, K. Motoya, M. Itoh, K. Inari, N. Eguchi, and J. Akimitsu, NMR and Neutron Scattering Studies of Quasi One-Dimensional Magnet CuV_2O_6 , *J. Phys. Soc. Jpn.* **69**, 2660 (2000).
- [51] Y. Yamada and A. Sakata, An analysis method of antiferromagnetic powder patterns in spin-echo NMR under external fields, *J. Phys. Soc. Jpn.* **55**, 1751 (1986).
- [52] M. Kontani, T. Hioki, and Y. Masuda, Hyperfine fields in an incommensurate antiferromagnetic Cr-Mo alloy system, *J. Phys. Soc. Jpn.* **39**, 672 (1975).
- [53] O. Janson, S. Chen, A. A. Tsirlin, S. Hoffmann, J. Sichelschmidt, Q. Huang, Z.-J. Zhang, M.-B. Tang, J.-T. Zhao, R. Kniep, and H. Rosner, Structure and magnetism of $\text{Cr}_2[\text{BP}_3\text{O}_{12}]$: Towards the quantum-classical crossover in a spin-3/2 alternating chain, *Phys. Rev. B* **87**, 064417 (2013).
- [54] O. Janson, G. Nénert, M. Isobe, Y. Skourski, Y. Ueda, H. Rosner, and A. A. Tsirlin, Magnetic pyroxenes $\text{LiCrGe}_2\text{O}_6$ and $\text{LiCrSi}_2\text{O}_6$: Dimensionality crossover in a nonfrustrated $S = \frac{3}{2}$ Heisenberg model, *Phys. Rev. B* **90**, 214424 (2014).
- [55] B. Lippold, J. Herrmann, W. Reichelt, and H. Oppermann, Preparation and magnetic investigations on $\text{Mn}_2\text{Mo}_3\text{O}_8$ single crystals, *phys. stat. sol. (a)* **121**, K91 (1990).
- [56] T. Kurumaji, S. Ishiwata, and Y. Tokura, Diagonal magnetoelectric susceptibility and effect of Fe doping in the polar ferrimagnet $\text{Mn}_2\text{Mo}_3\text{O}_8$, *Phys. Rev. B* **95**, 045142 (2017).
- [57] A. A. Tsirlin, R. Nath, J. Sichelschmidt, Y. Skourski, C. Geibel, and H. Rosner, Frustrated couplings between alternating spin- $\frac{1}{2}$ chains in AgVOAsO_4 , *Phys. Rev. B* **83**, 144412 (2011).